

Probing for high momentum protons in ${}^4\text{He}$ via the ${}^4\text{He}(e, e'p)X$ reaction

S. Iqbal,¹ F. Benmokhtar,^{2,*} M. Ivanov,³ N. See,¹ K. Aniol,¹ D. W. Higinbotham,⁴ C. Boyd,² A. Gadsby,² J. S. Goodwill,² D. Finton,² S. Gilad,⁵ A. Saha,^{4,†} J.M. Udias,⁶ Z. Ye,⁷ P. Solvignon,^{4,†} P. Aguilera,⁸ Z. Ahmed,⁹ H. Albataineh,¹⁰ K. Allada,⁴ B. Anderson,¹¹ D. Anez,¹² J. Annand,¹³ J. Arrington,⁷ T. Averett,¹⁴ H. Baghdasaryan,¹⁵ X. Bai,¹⁶ A. Beck,¹⁷ S. Beck,¹⁷ V. Bellini,¹⁸ A. Camsonne,⁴ C. Chen,¹⁹ J.-P. Chen,⁴ K. Chirapatpimol,¹⁵ E. Cisbani,²⁰ M. M. Dalton,^{15,4} A. Daniel,²¹ D. Day,¹⁵ W. Deconinck,⁵ M. Defurne,²² D. Flay,²³ N. Fomin,²⁴ M. Friend,²⁵ S. Frullani,²⁰ E. Fuchey,²³ F. Garibaldi,²⁰ D. Gaskell,⁴ R. Gilman,²⁶ S. Glamazdin,²⁷ C. Gu,¹⁵ P. Guèye,¹⁹ C. Hanretty,¹⁵ J.-O. Hansen,⁴ M. Hashemi Shabestari,¹⁵ M. Huang,²⁸ G. Jin,¹⁵ N. Kalantarians,²⁹ H. Kang,³⁰ A. Kelleher,⁵ I. Korover,³¹ J. LeRose,⁴ J. Leckey,³² R. Lindgren,¹⁵ E. Long,¹¹ J. Mammei,³³ D. J. Margaziotis,¹ P. Markowitz,³⁴ D. Meekins,⁴ Z. Meziani,²³ R. Michaels,⁴ M. Mihovilovic,³⁵ N. Muangma,⁵ C. Munoz Camacho,³⁶ B. Norum,¹⁵ Nuruzzaman,³⁷ K. Pan,⁵ S. Phillips,³⁸ E. Piassetzky,³¹ I. Pomerantz,³¹ M. Posik,²³ V. Punjabi,³⁹ X. Qian,²⁸ Y. Qiang,⁴ X. Qiu,⁴⁰ P. E. Reimer,⁷ A. Rakhman,⁹ S. Riordan,^{15,41} G. Ron,⁴² O. Rondon-Aramayo,^{15,4} L. Selvy,¹¹ A. Shahinyan,⁴³ R. Shneor,³¹ S. Sirca,^{44,35} K. Slifer,³⁸ N. Sparveris,²³ R. Subedi,¹⁵ V. Sulkosky,⁵ D. Wang,¹⁵ J. W. Watson,¹¹ L. B. Weinstein,⁴⁵ B. Wojtsekhowski,⁴ S. A. Wood,⁴ I. Yaron,³¹ X. Zhan,⁷ J. Zhang,⁴ Y. W. Zhang,²⁶ B. Zhao,¹⁴ X. Zheng,¹⁵ P. Zhu,⁴⁶ and R. Zielinski³⁸

(The Jefferson Lab Hall A Collaboration)

¹California State University, Los Angeles, Los Angeles, CA 90032

²Duquesne University, Pittsburgh, PA 15282

³Bulgarian Academy of Sciences, Bulgaria

⁴Thomas Jefferson National Accelerator Facility, Newport News, VA 23606

⁵Massachusetts Institute of Technology, Cambridge, MA 02139

⁶Compuense University de Madrid, Spain

⁷Physics Division, Argonne National Laboratory, Lemont, IL 60439

⁸Institut de Physique Nucléaire (UMR 8608), CNRS/IN2P3 - Université Paris-Sud, F-91406 Orsay Cedex, France

⁹Syracuse University, Syracuse, NY 13244

¹⁰Texas A&M University, Kingsville, TX 78363

¹¹Kent State University, Kent, OH 44242

¹²Saint Mary's University, Halifax, Nova Scotia, Canada

¹³University of Glasgow, Glasgow G12 8QQ, Scotland, United Kingdom

¹⁴College of William and Mary, Williamsburg, VA 23187

¹⁵University of Virginia, Charlottesville, VA 22904

¹⁶China Institute of Atomic Energy, Beijing, China

¹⁷Nuclear Research Center Negev, Beer-Sheva, Israel

¹⁸Università di Catania, Catania, Italy

¹⁹Hampton University, Hampton, VA 23668

²⁰INFN, Sezione Sanità and Istituto Superiore di Sanità, 00161 Rome, Italy

²¹Ohio University, Athens, OH 45701

²²CEA Saclay, F-91191 Gif-sur-Yvette, France

²³Temple University, Philadelphia, PA 19122

²⁴University of Tennessee, Knoxville, TN 37996

²⁵Carnegie Mellon University, Pittsburgh, PA 15213

²⁶Rutgers, The State University of New Jersey, Piscataway, NJ 08855

²⁷Kharkov Institute of Physics and Technology, Kharkov 61108, Ukraine

²⁸Duke University, Durham, NC 27708

²⁹Virginia Union University, Richmond, VA 23220

³⁰Seoul National University, Seoul, Korea

³¹Tel Aviv University, Tel Aviv 69978, Israel

³²Indiana University, Bloomington, IN 47405

³³Virginia Polytechnic Inst. and State Univ., Blacksburg, VA 24061

³⁴Florida International University, Miami, FL 33199

³⁵Jozef Stefan Institute, Ljubljana, Slovenia

³⁶Université Blaise Pascal/IN2P3, F-63177 Aubière, France

³⁷Mississippi State University, Mississippi State, MS 39762

³⁸University of New Hampshire, Durham, NH 03824

³⁹Norfolk State University, Norfolk, VA 23504

⁴⁰Lanzhou University, Lanzhou, China

⁴¹University of Massachusetts, Amherst, MA 01006

⁴²Racah Institute of Physics, Hebrew University of Jerusalem, Jerusalem, Israel

⁴³Yerevan Physics Institute, Yerevan 375036, Armenia

⁴⁴Faculty of Mathematics and Physics, University of Ljubljana, Ljubljana, Slovenia

⁴⁵Old Dominion University, Norfolk, VA 23529

⁴⁶University of Science and Technology, Hefei, China

(Dated: September 13, 2022)

Experimental cross sections for the ${}^4\text{He}(e, e'p)X$ reaction up to a missing momentum of 0.632 GeV/c at $x_B = 1.24$ and $Q^2 = 2(\text{GeV}/c)^2$ are reported. The data are compared to Relativistic Distorted Wave Impulse Approximation (RDWIA) calculations for ${}^4\text{He}(e, e'p)H$ channel. Significantly more events in the triton mass region are measured for $p_m > 0.45$ GeV/c than are predicted by the theoretical model, suggesting that the effects of initial-state multi-nucleon correlations are stronger than expected by the RDWIA model.

PACS numbers: 13.60.Hb, 25.10.+s, 25.30.Fj

I. INTRODUCTION

Nucleon momentum distributions in atomic nuclei are known to be governed by an average nuclear potential plus additional nucleon-nucleon and nucleon-multi-body interactions [1] [2]. Momentum distributions below the Fermi momentum essentially reflect the size of the “box” in which the nucleons are contained. One way to model this distribution is in the simplest limit of a cluster model where a given nucleon interacts with the average potential of the other nucleons. For momenta greater than the Fermi momentum, the cluster models of nuclear structure provide enhanced strength in the momentum distribution by allowing nucleon-nucleon spatial distributions to become shorter than the average nucleon-nucleon spacing.

Cross sections are critical observables to test ab initio calculations of nucleon momentum distributions. The large numbers of nucleon-nucleon data sets, [3], [4], based on neutron-proton or proton-proton reactions, are insufficient to account for the details of nucleon momentum distributions inferred from (e, e') inclusive electron scattering reactions, such as the proton-proton correlation function needed for the Coulomb sum rule, [5]. Two nucleon interactions also cannot explain, quantitatively, the binding energies of low mass nuclei, [3], [4]. Short range correlations between two nucleons and three body nucleon interactions are proposed to explain these observables. ${}^4\text{He}$ is the best nucleus to test theoretical nucleon momentum distributions because only four nucleons are involved in this many body problem and its central density is close to that of larger nuclei.

Microscopic nuclear structure calculations based on realistic two and three body nucleon-nucleon calculations are available for low mass nuclei [6]. In the case of ${}^4\text{He}$, proton momentum distributions have been calculated for proton-triton (pt) and deuteron-deuteron (dd) clusters. Recent measurements of proton-nucleon coincidences in the ${}^4\text{He}(e, e'p)N$ reaction [7–10] have shown strong correlations of back to back emission of nu-

cleon pairs for large missing momentum $p_m > 400$ MeV/c. Moreover, the increasing pair ratio $\frac{\#pp}{\#pn}$ as a function of $p_m > 400$ MeV/c is interpreted as a sign that the nucleon-nucleon interaction is evolving from the tensor interaction to the strong repulsive short range interaction.

Experimental access to proton momentum distributions in nuclei is possible through measurements of the differential cross section of the $A(e, e'p)X$ reaction and its dependence on the missing momentum p_m and the missing energy E_m . The $A(e, e'p)X$ reaction is illustrated in Fig. 1. Where $\vec{p}_X = \vec{p}_e - \vec{p}_{e'} - \vec{p}_p$, $p_m = |\vec{p}_X|$, is the momentum of the residual nucleus [11]. The missing energy, E_m , of the reaction is the excitation energy of the system; it is the difference between the electron transferred energy ($\omega = E_e - E_{e'}$) and the kinetic energies of the knocked out proton and the residual system, T_p and T_X , respectively: $E_m = \omega - T_p - T_X$. The energy of the beam electron is obtained from dedicated energy measurements, while the energies of the scattered electron and knocked out proton are deduced directly through their momenta measurements. The energy of the residual nucleus is calculated from its momentum; which is nothing other than the missing momentum of the reaction. Previous $(e, e'p)$ experiments were performed on different types of targets and as examples we cite here: [12, 13] on ${}^3\text{He}$, [14] on deuteron, [15] and ${}^{16}\text{O}$.

Differential cross section of proton knockout from ${}^4\text{He}$ have a history that started with electron beam energies below 1 GeV, as in Ref. [5]. But the low electron beam energy and accelerator facility, 560 MeV and small duty factor (1%), in that experiment limited the data to small $x_B \ll 1$ and missing momenta between 225 and 600 MeV/c. This paper provides experimental differential cross sections based on the ${}^4\text{He}(e, e'p)3N$ reaction over a range of missing momenta, $25 < p_m < 632$ MeV/c and $x_B = 1.24$, where $3N = {}^3\text{H}$ and X . The data was taken during the E08009 experiment in Hall A at Jefferson lab. These experimental results are compared to state-of-the-art Relativistic Distorted Wave Impulse Approximation (RDWIA) calculations of the Madrid group [16].

* Contact person benmokhtar@duq.edu

† deceased

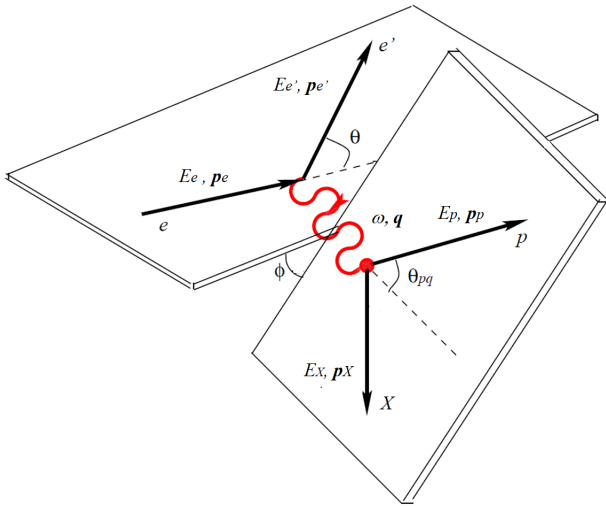


FIG. 1. Kinematic definitions for the $A(e, e'p)X$ reaction.

The remaining of this paper is divided as follows: In section II, the E08009 experimental setup is presented, explaining the spectrometer settings and the cryogenic target. Data analysis section is presented in section III, covering background subtractions, coincidence events selection, momentum acceptance efficiency, straggling and external bremsstrahlung. Details around the extraction of the cross section are presented in this section as well. In section IV cross section results are presented, where data is compared to the Madrid group's theoretical predictions. Following, a discussion and conclusion are presented in section V. Finally, an Appendix with tabulated experimental results and theoretical calculations are summarized in section VI.

II. EXPERIMENTAL SETUP

A. Spectrometer settings

Experiment E08009 [17] at the Thomas Jefferson National Accelerator Facility in experimental Hall A [18], ran in February, March and April of 2011, in parallel with the triple coincidence short-range correlation experiment described in Ref. [7]. Data for kinematic settings of 0.153 and 0.353 GeV/c missing momentum were obtained using electron beam currents between $47\mu A$ to $60\mu A$, for E08009. In addition to these kinematic settings the Short Range Correlation (SRC) [7] experiment also obtained data at kinematic settings out to 0.632 GeV/c missing momentum including the multi-body break up channel $p+3N$. These higher missing momenta data were collected using 4 to 5 μA electron beam currents but sufficient accumulated charge was measured to be able to extract cross sections beyond the original goal set for E08009. Moreover, the acceptances of the Hall A spectrometers allowed for cross sections to be determined

Central p_m GeV/c	θ_p deg.	θ_{pq} deg.	Central momentum GeV/c
0.153	47.0	-2.4	1.500
0.353	38.5	-10.9	1.449
0.466	33.5	-15.9	1.383
0.632	29.0	-20.4	1.308

TABLE I. Proton spectrometer settings

across a larger missing momentum range than the central value kinematic settings would suggest.

The electron spectrometer was fixed in angle and central momentum while the proton spectrometer's angles and central momenta were changed. Electron arm's kinematic settings for the experiment are as follows: incident beam energy 4.4506 GeV, electron spectrometer angle 20.3° electron spectrometer momentum 3.602 GeV/c, four momentum transfer $Q^2 = 2.0$ (GeV/c) 2 and Bjorken $x_b = 1.24$, 3 momentum transfer of 1.647 GeV/c at an angle $\theta_q = 49.4^\circ$ with respect to the incident electron momentum. The proton arm settings are in table I.

B. Cryogenic target

The cryogenic target was gas ^4He contained in an aluminum can of length 20 cm. The nominal temperature of the gas was 20° K at 199 psia. ^4He enters and exits at the upstream end of the target. There is no outlet for the fluid at the downstream end of the can. A determination of target density along the beam path was done by comparing the normalized yield of scattered electrons at $47\mu A$ and $60\mu A$ beam currents to the yield at $4\mu A$. Since the electron spectrometer was held at a fixed momentum and angle the electron spectrometer served as a density monitor. For this target at a beam current of $4\mu A$ a computational fluid dynamics (CFD) calculation [19] predicts an average density drop of 2.3% from strictly thermodynamic parameters. A comparison of the measured yield at $4\mu A$ to the CFD calculation gives an uncertainty in the target density dependence along the beam of 1.1%. More detail for the treatment of the target density used in the data analysis is available in [20]. Across the ± 8 cm effective target length and for the different beam currents, the target densities are summarized in table III.

III. DATA ANALYSIS

A. Background subtraction and coincidence event selection

For this experiment, event triggers were performed by coincident signals from scintillator arrays. Particle tracks were reconstructed using the high resolution spectrometer's vertical drift chambers. The small π^- back-

ground in the electron arm was rejected using a CO₂ gas Cherenkov detector. In the proton spectrometer, coincident π^+ , and other positively charged nuclei like ^2H , and ^3H were separated from the protons using the time difference between particles detected in the two spectrometers. Most of the accidental coincident events were rejected by cuts on the difference between interaction points in the target along the beam as reconstructed by the two spectrometers. The remaining accidental background was subtracted using the coincidence timing between the spectrometers. Fig. 2 shows a coincidence time of flight for the 353 MeV/c kinematics. The number of real coincidence events in a 20 ns time window around the peak was obtained by subtracting the accidentals under the peak considering a flat background under the whole spectrum, as shown in Fig. 2.

The wide momentum acceptance of the spectrometers allows for a broad missing momentum acceptance as shown in Fig. 3, so we were able to divide the study in 50 MeV/c wide bins in p_m . For each kinematical bin, the number of true coincidence events N_t determined from the coincidence time of flight with the formula:

$$N_t = N_0 - \frac{\Delta t_0(N_1 + N_2)}{\Delta t_1 + \Delta t_2} \quad (1)$$

where N_0 is the number of events within the bin reconstructing in the real coincidence window Δt_0 , and N_1 and N_2 are the number of events within the bin reconstructing in the accidental coincidence windows Δt_1 and Δt_2 , respectively. Statistical uncertainties were propagated as

$$\delta N_t = \sqrt{N_r + (N_1 + N_2)} \left(\frac{\Delta t_0}{\Delta t_1} + \Delta t_2 \right)^2 \quad (2)$$

For the determination of the cross section, the following phase-space cuts are applied to the data for both electron and proton spectrometers: horizontal angle ± 0.04 radians, vertical angle ± 0.03 radians, vertex position ± 8 cm and the deviation from central momentum $\pm 4.5\%$. These variables are shown in Fig. 4.

The full data set after accidental and background subtraction is presented in figure 5.

Data analysis is aided by the Monte Carlo simulation (GEANT 3.2 [21]) of the transport of the incident electron, scattered electron and proton through the target cell into the spectrometer apertures, assuming a p+triton final hadronic state. The identification of the p+triton final state is possible by calculating the missing energy in the scattered electron + p state. A peak in the missing energy spectrum, at 19.8 MeV, corresponding to the triton ground state identifies the $^4\text{He}(e, e'p)^3\text{H}$ reaction, as seen in figure 5.

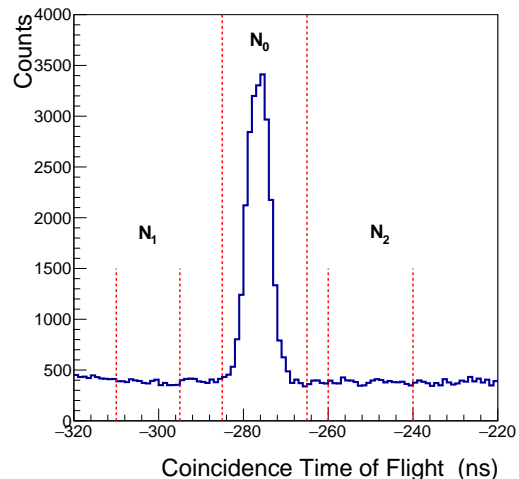


FIG. 2. Coincidence time of flight spectrum for the 353 MeV/c setting.

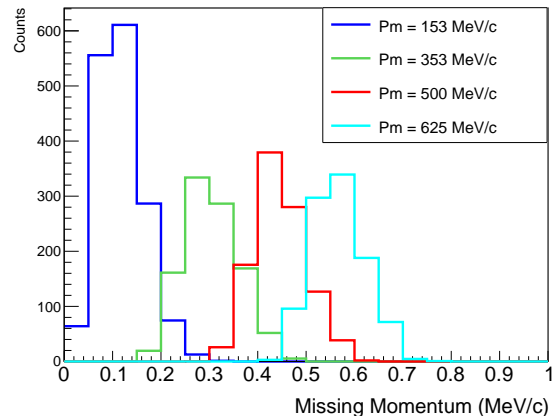


FIG. 3. Missing Momentum spectra for all the kinematical settings of the experiment.

B. Missing momentum acceptance efficiency

In the simulation a vertex point in the gas target is chosen which gives the incoming electron's momentum at interaction point. Then hit points within the apertures of the spectrometers for the outgoing electron and proton are randomly selected. Each point within the spectrometers' apertures has an equal probability of being selected. This allows for the vertex angles of the electron and proton to be determined. An energy for the outgoing electron is chosen within the momentum acceptance of the electron spectrometer. From the incident electron's momentum, the scattered electron's momentum and the angles for the ejected proton three body kinematics for the $^4\text{He}(e, e'p)^3\text{H}$ reaction allows for the proton's vertex momentum to be determined. The electron and proton are followed from the vertex to the final hit points in the spectrometers' apertures. Thus

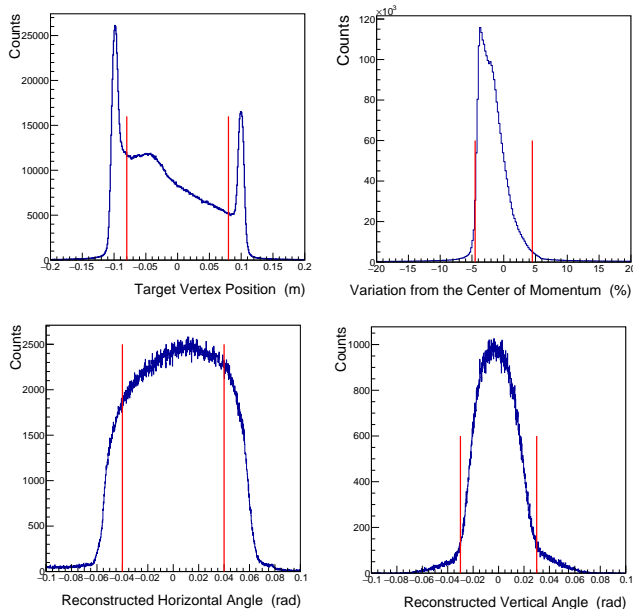


FIG. 4. Up left: Target vertex position in meters and up right: Variation from the central momentum %. Bottom left: reconstructed horizontal angle in radians, bottom right: Reconstructed vertical angle in radians.

complete information about the location and momenta at the vertex and the spectrometers' apertures is known.

The three body kinematical and geometrical limitations for particles arriving at the hit points within the apertures are calculated by GEANT and thus allows the missing momentum, $p_{\vec{m}} = \vec{p}_e - \vec{p}_{e'} - \vec{p}_p$ to be calculated. In the analysis we bin $|p_{\vec{m}}|$ into 50 MeV/c bins and we define the missing momentum acceptance factor, $f(p_m)$, for a bin as:

$$f(p_m) = \frac{n(p_m)}{\sum n(p_m)}. \quad (3)$$

where $n(p_m)$ is the number of triton events in the missing momentum bin centered on p_m and $\sum n(p_m)$ is the total number of triton events over all missing momenta for the particular proton kinematic setting. The same Gaussian broadening used for the simulation fit in figure 5 (b) is used to generate the values of p_m needed to calculate $f(p_m)$.

C. Peak broadening effects

Straggling and external bremsstrahlung obtained from the GEANT simulation produce a broadening and a characteristic tail on the missing energy spectrum. In practice the long target introduces additional broadening beyond the intrinsic point source resolution of the spectrometers. The additional broadening is included in

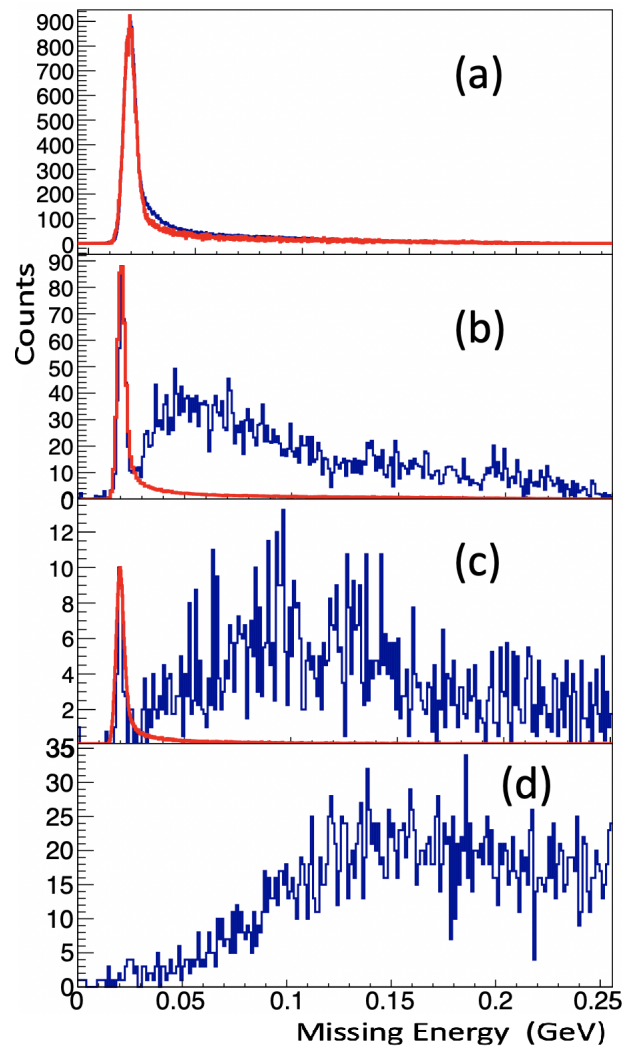


FIG. 5. Missing Energy spectra for all the kinematical settings. Data are in blue and the simulated two body breakup channel is in red. From top to Bottom: (a) $p_m = 153$ MeV/c, (b) $p_m = 353$ MeV/c, (c) $p_m = 466$ MeV/c and (d) $p_m = 632$ MeV/c

the simulation by a Gaussian smearing of the momenta at the apertures. It is typically a factor of three to four bigger than the resolution of the point source peak. The amount of Gaussian smearing needed is determined by the best fit of a strong missing energy data peak such as at the lowest missing momentum. An example of the fit is seen in figure 5(b). Where the simulation of the two body break-up channel is represented in red.

D. Extraction of the Cross Section

The average cross section for the ${}^4\text{He}(e, e'p)X$ reaction per missing momentum bin was extracted for the triton region and it is given by:

$$\langle \sigma(p_m) \rangle = \frac{n(p_m) * RSC}{\Delta\Omega_e \Delta\Omega_p \Delta E_e N_e N_{tgt} * Eff} \quad (4)$$

where:

- a) $n(p_m)$ is the net counts in the triton region between missing energies of 0.017 GeV to 0.022 GeV, after randoms and background subtraction. The three nucleon region, 3N, lies between 0.017 GeV and 0.029 GeV in the missing energy spectrum. Background subtraction in the triton region was done using straight line background below 0.029 GeV. An example of this background subtraction for 353 MeV/c kinematics is shown in Fig. 6.

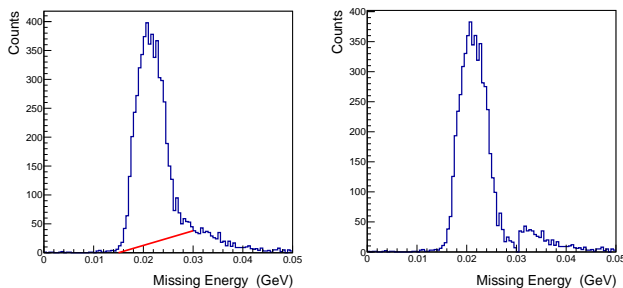


FIG. 6. Missing energy spectrum for the 153 MeV/c kinematics. Left: before straight line background subtraction and showing the position of the line in red. Right: After the straight line background subtraction.

- b) RSC is the radiative and straggling corrections to the cross section due to the tail on the missing energy spectrum. These corrections are determined by comparing the number of events in a 5 MeV window centered on the triton peak to the total number of events in the GEANT simulation. There is little variation in RSC from the simulation between proton spectrometer settings: $1.33 < SRC < 1.35$. There is an uncertainty of 0.2% on RSC.
- c) $\Delta\Omega_e$ and $\Delta\Omega_p$ are the geometrical solid angles of the spectrometer apertures.
- d) ΔE_e is the size of the electron's momentum bin in coincidence with protons; it is the proton arm that determines ΔE_e . A two dimensional plot of proton momentum versus electron momentum for the total coincidence events is presented in Fig.7 for the 153 MeV/c kinematics. Plots for higher momenta look similar with less statistics. This plot was then studied for various missing momentum bins for a given kinematics. This reduces the statistics making the choice of ΔP somehow ambiguous. Therefore, an uncertainty of 10% was attributed to ΔE_e .
- e) $N_e = Q/e$, the number of electrons that passed through the target, where e is the electron charge

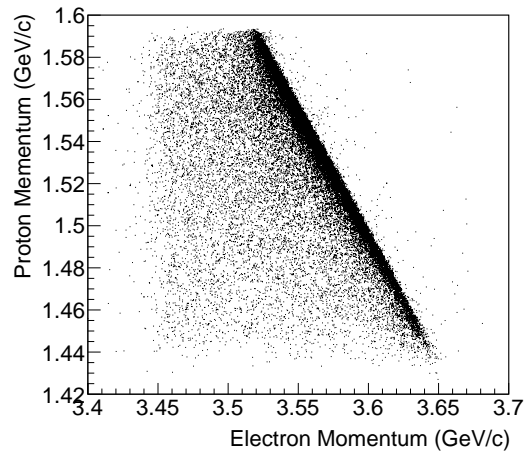


FIG. 7. Proton momentum versus electron momentum for the 153 MeV/c kinematics.

and Q is the total charge. This number was known to 0.3 to 0.5 %.

- f) $N_{tgt} = \rho(I) * z_{tgt}$ is the number of nuclei per cm² in the beam. I is the beam current, $\rho(I)$ is the number of nuclei per cm³ and z_{tgt} is the effective target length. Target densities along the ± 8 cm effective target length for different beam currents are presented in table III. N_{tgt} was known to 1.14%.
- g) Eff is the efficiency factor and it accounts for:

1. a missing momentum acceptance factor (ACC) (explained in section III B),
2. data acquisition live time (LTdaq),
3. electronics live time (LTel),
4. trigger efficiency (Tri),
5. wire chamber (WC) and
6. tracking efficiencies (Tra).

This Efficiency is given by:

$$Eff = ACC \cdot LTd \cdot LTe \cdot Tri \cdot WC \cdot Tra \quad (5)$$

The live time of the trigger acquisition system, $LTdaq$, was 0.916 ± 0.01 , and 0.95 ± 0.01 for the 153 MeV/c and 353 MeV/c kinematics, respectively. For the higher missing momentum settings, $LTdaq$ was larger than 0.99. The remaining efficiencies are displayed in table IV.

electronic livetime	1	0
trigger efficiency	0.97	0.01
wire chamber efficiency	0.995	0.001
tracking efficiency	0.9895	0.0075

TABLE II. General uncertainties

Experimental cross section results are presented in table V.

Beam current (μA)	Target density $\text{nuclei}/\text{cm}^2$
4.014	$7.84 \pm 0.087 \times 10^{22}$
45.46	$6.732 \pm 0.077 \times 10^{22}$
60.71	$5.662 \pm 0.065 \times 10^{22}$

TABLE III. Target density dependence on beam heating as a function of beam current.

Efficiency	value	Uncertainty (%)
Electronic live time	1	0
Trigger efficiency	0.97	1
Wire chamber efficiency	0.995	0.1
Tracking efficiency	0.9895	0.75

TABLE IV. General uncertainties

IV. RESULTS

A. Comparison of data to theoretical predictions

Experimental differential cross sections are compared to relativistic distorted wave impulse approximation calculations of the Madrid theory group [16, 22–24]. The ^4He ground state is described by a relativistic solution of the Dirac equation phenomenologically adjusted to fit the observed radius and binding energy of ^4He . These calculations were first introduced in [25].

Vertex values of the incident electron’s momentum at various positions within the target and the momenta of the scattered electron and ejected proton were provided to the Madrid theory group for calculation of the cross section at each event vertex in the GEANT simulation. The GEANT simulation also contains the detected electron and proton momenta at the spectrometers’ apertures. In this way the vertex cross section can be associated with the missing momentum at the apertures.

Theoretical cross sections integrated over the experimental acceptances for the full Madrid treatment and using the effective momentum approximation, EMA, treatment are presented in tables VI and VII. Plots of the data for the two theoretical treatments are shown in figures 8 and 9.

Data and calculations show the same missing momenta dependence for the measured or calculated cross section as a function of kinematic setting. Even though the same magnitude of p_m is reached for different proton angles the cross section does not simply factor as a function of p_m . Good agreements between the Madrid calculation and the data extend to about 420 MeV/c in missing momentum. It can be also noticed that both data and theory exhibit an inflection in the slope of the cross section between 300 and 400 MeV/c. In recent calculations on light

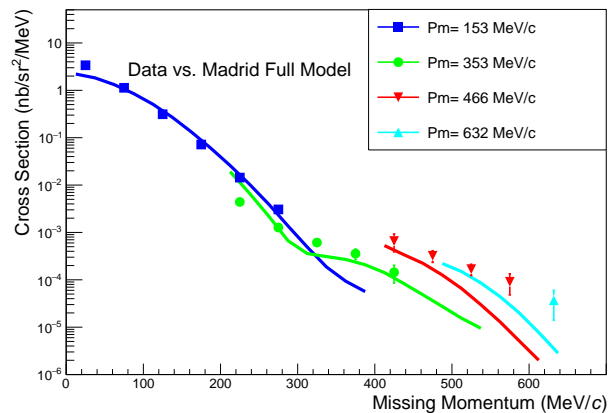


FIG. 8. E08009 Data compared to Madrid full theoretical calculations. Blue squares are for the 153 MeV/c setting, green circles are for the 353 MeV/c setting, red inverted triangles are for the 466 MeV/c setting and cyan triangles are for the 632 MeV/c setting. Theoretical calculation follow the same color code as the data for each momentum setting.

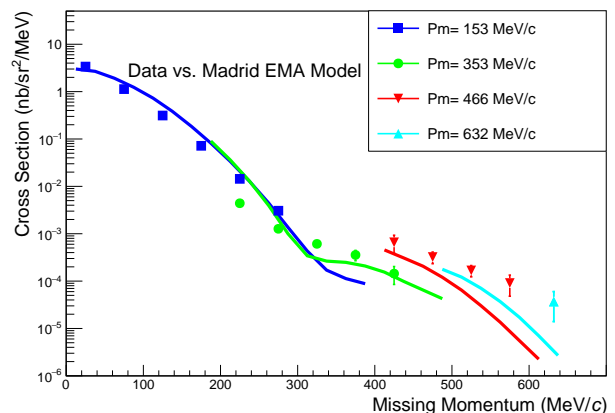


FIG. 9. E08009 Data compared to Madrid EMA theoretical calculations. Blue squares are for the 153 MeV/c setting, green circles are for the 353 MeV/c setting, red inverted triangles are for the 466 MeV/c setting and cyan triangles are for the 632 MeV/c setting. Theoretical calculation follow the same color code as the data for each momentum setting.

nuclei [6], an inflection in the proton momentum distributions was predicted in the momentum range between 1 and 3 fm $^{-1}$. For ^4He , this inflection appears to be due to the triton+proton cluster distribution exhibiting a deep minimum in the proton momentum distribution. When added to the deuteron cluster distribution, the inflection appears below and close to 2 fm $^{-1}$ in the total proton density distribution, which is in agreement with the one we see in these data.

V. DISCUSSION AND CONCLUSION

For this experiment, the three momenta of the outgoing proton and scattered electron in the $^4\text{He}(e, e'p)X$

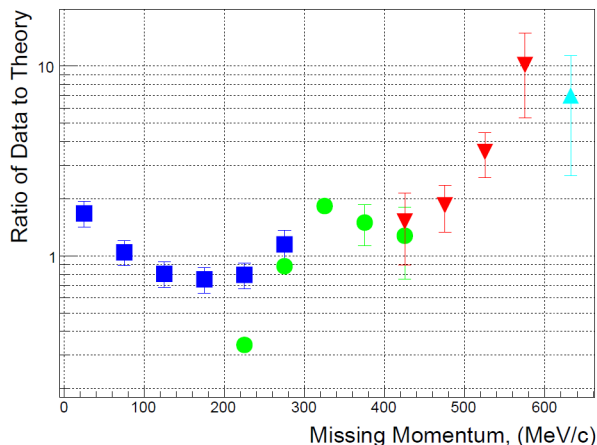


FIG. 10. Ratio of the experimental cross section to the theoretical Madrid full (pt) cross section versus missing momentum. Squares are for the 153 MeV/c setting, circles are for 353 MeV/c setting, inverted triangles are for the 466 MeV/c setting and triangles are for the 632 MeV/c setting.

reaction are measured. Using the known momentum of the initial state we deduce the missing momentum of the residual hadronic state X . The theoretical analysis of the data here is limited to a specific exit channel, $X = {}^3\text{H}$. However, considering the theoretical cluster contributions to the proton momenta [6] in ${}^4\text{He}$, the contribution of the pt cluster to the proton momentum distribution is expected to be negligible above about $p_m = 250$ MeV/c.

The ratio of experimental cross section to the Madrid full predictions; in logarithmic scale, is shown in figure 10 for the four proton spectrometer central momentum settings. The blue squares, at the lowest missing momentum setting, hover around a ratio of 1, showing good agreement between data and predictions. The green dots are for the 0.353 GeV/c setting and we see a distinctive pattern for these data. The ratio at 0.225 GeV/c is 0.34, substantially different from the model prediction. This behavior cannot be traced to a statistical fluctuation because as we see in figure 5 (b), there is a substantial peak at the triton missing energy location. The cross section decreases by a factor of 12 between 0.225 and 0.325 GeV/c and over the full range in missing momentum for this proton angle setting the cross section falls by a factor of 30. This fluctuation of the data to theory ratio suggests that some significant physics is not adequately included in the theoretical model for this range of missing momentum with these spectrometer settings. For the data at the 0.466 and 0.632 GeV/c settings the ratio again shows a smooth missing momentum dependence.

However, the overall dependence of the cross section by the Madrid full model in figure 8 is qualitatively described.

From [6], the high proton momentum is attributed to the repulsive nucleon-nucleon core. Fig. 5 shows a

broad peak in the missing energy spectrum which shifts in position kinematically with the photon being absorbed on a correlated pair of nucleons. This feature has been previously seen in ${}^3\text{He}(e, e'p)pn$ measurements in Ref. [12] and [26] and in ${}^4\text{He}(e, e'p)X$ continuum channel in Ref. [5].

The measurements of [7] are consistent with the NN short range force becoming repulsive. However, it is counter intuitive and in disagreement with theoretical expectations [6] that tritons should be ejected from ${}^4\text{He}$ along with protons emerging from short range encounters.

The fact that we observe events in the triton region up to 632 MeV/c involves processes beyond the impulse approximation. Final state interactions of the outgoing proton may take a proton knocked out of a pt cluster initially at a low value of p_p to appear as if its momentum at the vertex was p_m . This is accounted for to some extent by the optical model potential treatment of the final pt unbound state. We see good agreement between the theory and data in figure 8 up to about $p_m = 420$ MeV/c.

Beyond about 450 MeV/c in p_m substantially more triton region events are measured than what the Madrid full theory predicts. In this case three nucleons emitted at high p_m may be a signature of other reactions allowing the three nucleon cluster to emerge as a bound or quasi bound state. Since the kinematics for the electron were chosen for $x_b = 1.24$, protons in more intimate interactions with neighbors than quasi-elastic conditions ($x_b \approx 1$) may favor other reactions leading to three nucleon clusters exiting in the missing energy region near the triton.

Portions of the missing energy spectrum in the triton energy range are shown in figures 11. We see a change in the distribution of events as a function of missing momentum going from 153 MeV/c to 575 MeV/c. At low missing momenta the triton peak is centered at the expected value of 19.8 MeV. At higher missing momenta, the event are higher in missing energy by few MeVs. From left to right, the three arrows in each figure point to the expected locations of the thresholds of the hadronic states $X=(t)$, $X=(n,d)$ and $X=(p,n,n)$, respectively.

An interesting question is the impact of three-nucleon forces, V_{ijk} , at high p_m . V_{ijk} are known to increase the binding energy of nuclei [3] so they would be natural actors in the formation of bound tritons or closely bound three nucleon groups among the outgoing hadronic channels, X , at high missing momentum. The principal sources of data to help refine models of possible three-nucleon interactions are binding energies of ground and excited states of $A < 8$ nuclei and point proton charge distributions [3]. However, these data are not extensive enough to select unambiguously a particular set of parameters or models for V_{ijk} and other observables are needed as discussed in [3] [4].

More extensive and detailed data in the three nucleon triton mass region and the existence of microscopic calcu-

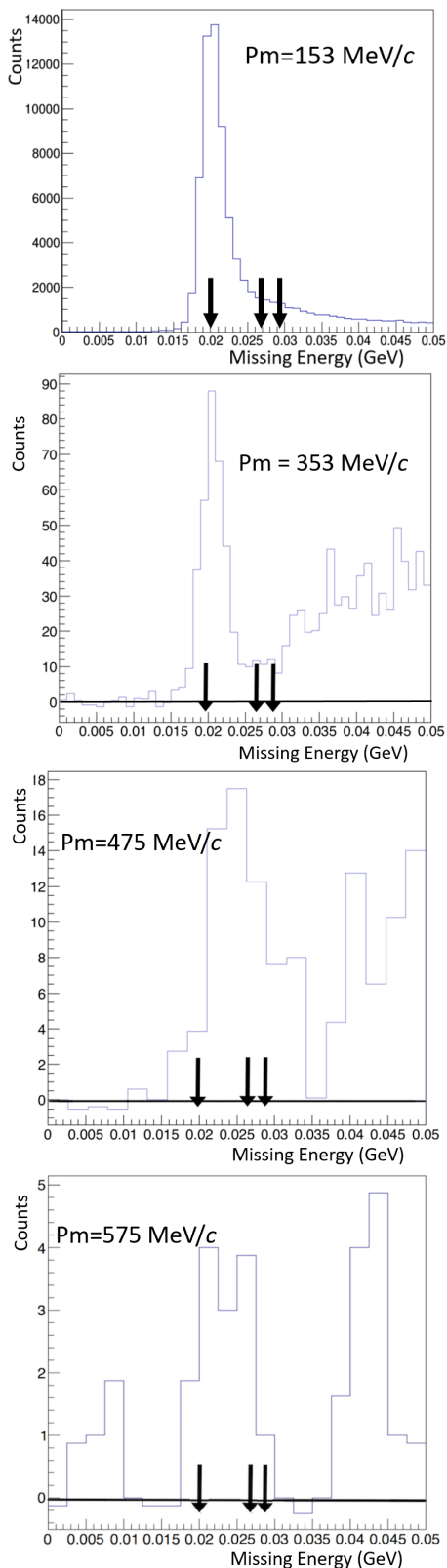


FIG. 11. From top to bottom: Missing energy region up to 50 MeV of excitation in ${}^4\text{He}(e, e'p)X$ for $p_m=153$, 352, 475 and 575 MeV/c, respectively. The three arrows point to the expected locations of the thresholds of the hadronic states $X=(t)$, $X=(n,d)$ and $X=(p,n,n)$.

lations for these nuclei opens the possibility of exploiting the shapes of the missing energy spectra in $A(e, e'p)X$ reactions as additional observables for developing models of three-nucleon interactions.

ACKNOWLEDGMENTS

Special thanks to Silviu Covrig for providing the CFD calculations as a possibility to understanding the target vertex spectra for the SRC Target. Special thanks to Or Hen for valuable discussions and inputs on the paper. The research presented in this paper is partially supported by the U.S. National Science Foundation grants PHY 09-69380 and PHY 16-15067. This work was supported by the U.S. Department of Energy contract DE-AC05-06OR23177 under which Jefferson Science Associates operates the Thomas Jefferson National Accelerator Facility.

VI. APPENDIX

Experimental differential cross sections for ${}^4\text{He}(e, e'p)X$; in $nb/sr^2/MeV$, are summarized in table V for the four different spectrometer settings. The analysis was done on 50 MeV/c wide bins on missing momentum, p_m . Errors are both statistics and systematics added in quadrature. The systematic uncertainty of 10% was included in the cross sections due to defining the size of the energy window, ΔE_e , on the electron spectrum.

Tables VII and VI summarize the Madrid EMA and full calculations respectively in the momentum range from 12.5 to 637.5 MeV/c.

p_m (MeV/c)	153 $\theta_p = 47^\circ$	353 $\theta_p = 38.5^\circ$	466 $\theta_p = 33.5^\circ$	632 $\theta_p = 29^\circ$
25	(3.38 ± 0.52)			
75	(1.13 ± 0.17)			
125	$(3.13 \pm 0.48) \times 10^{-1}$			
175	$(7.18 \pm 1.1) \times 10^{-2}$			
225	$(1.44 \pm 0.22) \times 10^{-2}$	$(4.40 \pm 0.14) \times 10^{-3}$		
275	$(3.06 \pm 0.57) \times 10^{-3}$	$(1.27 \pm 0.03) \times 10^{-3}$		
325		$(6.11 \pm 0.14) \times 10^{-4}$		
375		$(3.57 \pm 0.88) \times 10^{-4}$		
425		$(1.44 \pm 0.59) \times 10^{-4}$	$(6.59 \pm 2.7) \times 10^{-4}$	
475			$(3.22 \pm 0.89) \times 10^{-4}$	
525			$(1.68 \pm 0.45) \times 10^{-4}$	
575			$(0.91 \pm 0.43) \times 10^{-4}$	
632				$(3.7 \pm 2.3) \times 10^{-5}$

TABLE V. Experimental differential cross sections, $\frac{d\sigma^5}{d\Omega_p d\Omega_e dE_e}$, for ${}^4\text{He}(e, e'p)X$; where $X = {}^3\text{H}$ or ${}^3\text{N}$, from E08009, for different kinematical settings given by the proton spectrometer central angle. Units are $\text{nb}/\text{sr}^2/\text{MeV}$.

-
- [1] J. J. Kelly, *Adv. Nucl. Phys.* **23** (2002).
- [2] M. M. Sargsian *et al.*, *J. Phys.* **G29**, R1 (2003), arXiv:nucl-th/0210025 [nucl-th].
- [3] S. C. Pieper, V. R. Pandharipande, R. B. Wiringa, and J. Carlson, *Phys. Rev. C* **64**, 014001 (2001).
- [4] D. Lonardonì, A. Lovato, S. C. Pieper, and R. B. Wiringa, *Phys. Rev. C* **96**, 024326 (2017).
- [5] J. M. LeGoff, *et al.*, *Phys. Rev. C* **50**, 2278 (1994).
- [6] R. B. Wiringa, R. Schiavilla, S. C. Pieper, and J. Carlson, *Phys. Rev. C* **89**, 024305 (2014).
- [7] I. Korover, *et al.*, *Phys. Rev. Lett.* **113**, 022501 (2014).
- [8] R. Schiavilla, R. B. Wiringa, S. C. Pieper, and J. Carlson, *Phys. Rev. Lett.* **98**, 132501 (2007), arXiv:nucl-th/0611037 [nucl-th].
- [9] M. M. Sargsian, T. V. Abrahamyan, M. I. Strikman, and L. L. Frankfurt, *Phys. Rev. C* **71**, 044615 (2005), arXiv:nucl-th/0501018 [nucl-th].
- [10] M. Alvioli, C. Ciofi degli Atti, and H. Morita, *Phys. Rev. Lett.* **100**, 162503 (2008).
- [11] J. J. Kelly, *Adv. Nucl. Phys.* **23**, 75 (1996).
- [12] F. Benmokhtar, *et al.*, *Phys. Rev. Lett.* **94**, 082305 (2005).
- [13] M. Ravachev, *et al.*, *Phys. Rev. Lett.* **94**, 192302 (2005).
- [14] W. Boeglin, *et al.*, *Phys Rev Lett* **26**, 26501 (2011).
- [15] N. Liyanage, *et al.*, *Phys. Rev. Lett* **86**, 5670 (2001).
- [16] J. M. Udias, J. R. Vignote, E. Moya de Guerra, A. Escuderos, and J. A. Caballero, in *5th Workshop on Electromagnetically Induced Two Hadron Emission Lund, Sweden, June 13-16, 2001* (2001) arXiv:nucl-th/0109077 [nucl-th].
- [17] E08009 experimental proposal: A. Aniol, F. Benmokhtar, S. Gilad and H. Higinbotham https://www.jlab.org/exp_prog/CEBAF_EXP/E08009.html.
- [18] J. Alcorn *et al.*, *Nucl. Instrum. Meth.* **A522**, 294 (2004).
- [19] Silviu Covrig, Computational Fluid Dynamics, private communication (2012).
- [20] Sophia Iqbal California State University, Los Angeles 2013, DOE/OR/23177-3086, https://misportal.jlab.org/ul/publications/view_pub.cfm?pub_id=13189.
- [21] Instructions for COMGEANT, <https://userweb.jlab.org/~gen/simul/>, unpublished.
- [22] S. P. Malace, *et al.* *Phys. Rev. Lett.* **106**, 052501 (2011).
- [23] R. Álvarez Rodríguez, *et al.*, *Few-Body Systems* **50**, 359 (2011).
- [24] J. M. Udias and J. R. Vignote, *Phys. Rev. C* **62**, 034302 (2000).
- [25] M. Paolone, *et al.*, *Phys. Rev. Lett.* **105**, 072001 (2010).
- [26] C. Marchand, *et al.*, *Phys. Rev. Lett* **60**, 1703 (1988).

p_m (MeV/c)	153 $\theta_p = 47^\circ$	353 $\theta_p = 38.5^\circ$	466 $\theta_p = 33.5^\circ$	632 $\theta_p = 29^\circ$
12.5	2.2059			
37.5	1.8287			
62.5	1.3139			
87.5	8.516e-01			
112.5	5.070e-01			
137.5	2.699e-01			
162.5	1.311e-01			
187.5	5.987e-02			
212.5	2.583e-02	1.918e-02		
237.5	1.044e-02	6.724e-03		
262.5	3.951e-03	2.209e-03		
287.5	1.370e-03	6.686e-04		
312.5	4.901e-04	3.578e-04		
337.5	1.858e-04	3.095e-04		
362.5	9.309e-05	2.687e-04		
387.5	5.639e-05	2.077e-04		
412.5		1.419e-04	5.283e-04	
437.5		8.366e-05	3.402e-04	
462.5		4.808e-05	2.225e-04	
487.5		2.739e-05	1.262e-04	2.206e-04
512.5		1.542e-05	6.542e-05	1.491e-04
537.5		9.478e-06	2.980e-05	8.585e-05
562.5			1.289e-05	4.400e-05
587.5			5.077e-06	1.977e-05
612.5			2.008e-06	7.741e-06
637.5			8.357e-07	2.834e-06

TABLE VI. Madrid full theoretical cross sections integrated over the experimental acceptances for ${}^4\text{He}(e, e'p){}^3\text{H}$ for E08009, for different kinematical settings given by the proton spectrometer central angle. Units are $nb/sr^2/MeV$.

p_m (MeV/c)	153 $\theta_p = 47^\circ$	353 $\theta_p = 38.5^\circ$	466 $\theta_p = 33.5^\circ$	632 $\theta_p = 29^\circ$
37.5	2.681			
62.5	1.916			
87.5	1.235			
112.5	7.297e-01			
137.5	3.839e-01			
162.5	1.834e-01			
187.5	8.159e-02	9.031e-02		
212.5	3.382e-02	3.628e-02		
237.5	1.282e-02	1.295e-02		
262.5	4.433e-03	3.933e-03		
287.5	1.362e-03	9.986e-04		
312.5	4.312e-04	3.423e-04		
337.5	1.705e-04	2.643e-04		
362.5	1.130e-04	2.487e-04		
387.5	8.817e-05	2.083e-04		
412.5		1.547e-04	4.550e-04	
437.5		9.853e-05	3.082e-04	
462.5		6.482e-05	2.064e-04	
487.5		4.261e-05	1.206e-04	1.778e-04
512.5			6.435e-05	1.215e-04
537.5			3.036e-05	7.084e-05
562.5			1.360e-05	3.702e-05
587.5			5.527e-06	1.717e-05
612.5			2.251e-06	7.010e-06
637.5			9.483e-07	2.695e-06

TABLE VII. Madrid EMA theoretical cross sections integrated over the experimental acceptances for ${}^4\text{He}(e, e'p){}^3\text{H}$ for E08009, for different kinematical settings given by the proton spectrometer central angle. Units are $nb/sr^2/MeV$.